

A Wave Model and Diffusion Coefficients for Plasmaspheric Hiss Parameterized by Plasmopause Location

David M. Malaspina¹, Hui Zhu², and Alexander Yurievich Drozdov³

¹University of Colorado Boulder

²University of Texas at Dallas

³University of California Los Angeles

November 21, 2022

Abstract

The scattering of electrons via plasmaspheric hiss whistler-mode plasma waves has profound consequences for the dynamics of electrons in the inner terrestrial magnetosphere, including the radiation belts. Consequently, simulations of inner magnetospheric electron dynamics incorporate hiss wave models, though these models are often parameterized by quantities convenient to describe particle populations (e.g. L-shell). However, recent studies have revealed that the spatial distribution of plasmaspheric hiss wave power is only weakly dependent on L-shell. Instead, it is dictated by the density structure of the plasmasphere (including radial extent and azimuthal structure). In this work, we create a plasmaspheric hiss wave model, and corresponding particle diffusion coefficients, parameterized by plasmopause location instead of L-shell, in order to quantify the importance of including plasmopause-organization of hiss waves for inner magnetosphere models. Significant differences in electron scattering lifetimes are found when comparing L-shell parameterized hiss and plasmopause-parameterized hiss wave models on the timescales of days. This implies that plasmopause-parameterization of hiss waves may be important for modeling specific geomagnetic events.

1 **A Wave Model and Diffusion Coefficients for**
2 **Plasmaspheric Hiss Parameterized by Plasmopause**
3 **Location**

4 **David M. Malaspina ¹, Hui Zhu ², Alexander Drozdov ³**

5 ¹Laboratory for Atmospheric and Space Physics, University of Colorado, Boulder, Colorado, USA

6 ²University of Texas at Dallas, Dallas, Texas, USA

7 ³University of California, Los Angeles, Los Angeles, California, USA

8 **Key Points:**

- 9 • An observation-based wave model for plasmaspheric hiss parameterized by plasma-
- 10 pause location is created
- 11 • Corresponding diffusion coefficients are calculated
- 12 • Differences between wave models parameterized by plasmopause location and by
- 13 L-shell are demonstrated via simulations of an idealized storm

Abstract

The scattering of electrons via plasmaspheric hiss whistler-mode plasma waves has profound consequences for the dynamics of electrons in the inner terrestrial magnetosphere, including the radiation belts. Consequently, simulations of inner magnetospheric electron dynamics incorporate hiss wave models, though these models are often parameterized by quantities convenient to describe particle populations (e.g. L-shell). However, recent studies have revealed that the spatial distribution of plasmaspheric hiss wave power is only weakly dependent on L-shell. Instead, it is dictated by the density structure of the plasmasphere (including radial extent and azimuthal structure). In this work, we create a plasmaspheric hiss wave model, and corresponding particle diffusion coefficients, parameterized by plasmopause location instead of L-shell, in order to quantify the importance of including plasmopause-organization of hiss waves for inner magnetosphere models. Significant differences in electron scattering lifetimes are found when comparing L-shell parameterized hiss and plasmopause-parameterized hiss wave models on the timescales of days. This implies that plasmopause-parameterization of hiss waves may be important for modeling specific geomagnetic events.

1 Introduction

Plasmaspheric hiss is a broadband superposition of whistler-mode plasma waves located within and nearby the plasmasphere, a torus of cold plasma surrounding Earth. Hiss scatters electrons in pitch angle, facilitating their loss to the atmosphere and thereby playing a significant role in shaping inner magnetospheric electron populations, including relativistic radiation belt electrons (e.g. see Millan & Thorne, 2007). For this reason, electron loss by hiss wave scattering is a critical component of simulations of the inner magnetosphere (Albert et al., 2009; Fok et al., 2014; Jordanova & Miyoshi, 2005; Miyoshi et al., 2006; Shprits et al., 2008; Subbotin & Shprits, 2009). Simulations often include the physics of hiss-induced particle scattering using statistical maps of hiss wave characteristics (e.g. intensity, spectral shape) parameterized by L-shell, magnetic local time (MLT), and geomagnetic activity level (Glauert et al., 2014; Meredith et al., 2007; Orlova et al., 2014; Tsurutani et al., 2015; Orlova et al., 2016).

Recent studies have demonstrated (Malaspina et al., 2016, 2017) that the plasmasphere plays a larger role in the distribution of plasmaspheric hiss wave power than sim-

45 ply acting as an outer boundary to wave occurrence (as in Meredith et al. (2007), for ex-
 46 ample). Instead, it was found that the distribution of hiss wave power dynamically adapts
 47 to the shape of the plasmasphere, with the peak hiss intensity consistently located a dis-
 48 tance of 1 to 1.5 L-shell Earthward of the plasmopause. Further, Malaspina, Ripoll, Chu,
 49 Hospodarsky, and Wygant (2018) demonstrated that the radial variation in hiss wave
 50 power is determined by primarily by plasma density and is only weakly related to L-shell.

51 The finding that hiss waves do not follow the L-shell parameterization that mod-
 52 els often assume may be of critical importance for physically accurate modeling of wave-
 53 particle interactions by hiss waves in the inner magnetosphere. If the hiss wave power
 54 peak is being modeled at an unphysical location and/or with an unphysical amplitude,
 55 particle scattering estimates may be significantly affected. Further, the shape of the plas-
 56 masphere, and therefore the spatial distribution of hiss wave power, is constantly evol-
 57 ving, dynamically determined by a balance of solar wind-driven convection, co-rotation
 58 with Earth’s magnetic field, refilling from ionospheric outflow, and the time history of
 59 all these processes (Carpenter & Lemaire, 2004).

60 In this work, we begin quantifying the difference between hiss parameterized by plasma-
 61 pause location (L_{pp} -sorted) and hiss parameterized by L-shell (L -sorted) for models of
 62 hiss wave scattering by: (i) Using Van Allen Probes plasma wave observations to cre-
 63 ate a database of hiss wave power parameterized by wave frequency, magnetic local time,
 64 plasmopause location (using both L_{PP} , the distance of the plasmopause from Earth, and
 65 ΔL_{PP} , the distance from the plasmopause), and the Kp geomagnetic index. (ii) Using
 66 this observational database to produce a L_{pp} -sorted hiss wave model amenable to cal-
 67 culation of diffusion coefficients. (iii) Producing diffusion coefficients based on the wave
 68 model. (iv) Applying the L -sorted and L_{pp} -sorted diffusion coefficients to model an ide-
 69 alized geomagnetic storm using the Versatile Electron Radiation Belt (VERB) code (Subbotin
 70 & Shprits, 2009), performing one-dimensional pitch-angle diffusion simulations, and com-
 71 paring code outputs.

72 This work focuses on plasmaspheric hiss, defined here as hiss found within the plas-
 73 masphere at frequencies between 150 Hz and ~ 2 kHz. Other hiss types will be param-
 74 eterized in future work, including plume hiss (Li et al., 2019), low frequency hiss (Li et
 75 al., 2013), lightning hiss (Meredith et al., 2007), and exohiss (Zhu et al., 2015; Zhu et
 76 al., 2019). By building a wave model for each hiss type separately, they can be included

77 or excluded from VERB code runs to quantify their relative importance to inner mag-
78 netospheric dynamics.

79 Section 2 describes the wave data and its processing. Section 3 describes the pa-
80 rameterized wave model built from the observations. Section 4 describes the calculation
81 of diffusion coefficients, and Section 5 treats the VERB modeling. Conclusions are pre-
82 sented in Section 6.

83 **2 Observations**

84 **2.1 Data Set Creation**

85 This study uses data from the Van Allen Probes mission (Mauk et al., 2013). These
86 two identical spacecraft have elliptical orbits about the Earth with perigee near 600 km
87 and apogee near 6 Earth radii (R_E). Their orbits are within 20° of the geomagnetic equa-
88 tor and each has an orbital period close to 9 hours. Over ~ 2 years, their orbital line of
89 apsides precesses through all MLT. The spacecraft are spin-stabilized with ~ 11 s spin
90 period.

91 Instrument data used in this study are from the Electric Fields and Waves (EFW)
92 instrument (Wygant et al., 2013) and the Electric and Magnetic Field Instrument Suite
93 and Integrated Science (EMFISIS) suite (Kletzing et al., 2013). These instruments record
94 and process measurements made by six electric field probes, a three-axis search coil mag-
95 netometer (SCM), and a three-axis fluxgate magnetometer (FGM). The data products
96 used by this study include the spacecraft potential (32 Samples/s), the DC-coupled mag-
97 netic field (64 Samples/s), density determined from a combination of the upper hybrid
98 frequency (1 sample / 6.5 s) and spacecraft potential, and on-board calculated wave power
99 spectra of each SCM axis (65 pseudo-logarithmically spaced frequency bins from ~ 2 Hz
100 to ~ 12 kHz, 1 spectra / 6s). Wave planarity and ellipticity data, derived from on-board
101 calculated cross-spectral data (1 spectra / 6s), are also used.

102 Data from both Van Allen Probes are used. For Van Allen Probe B, data from 01
103 November, 2012 through 31 January, 2018 are used. For Van Allen Probe A, data from
104 01 November, 2012 through 31 May, 2016 are used. Data after May 2016 on Van Allen
105 Probe A are not used, as accumulated radiation damage to that spacecraft's electric field
106 sensor preamplifiers compromised their ability to accurately measure spacecraft poten-
107 tial soon after that date.

108 The Olson-Pfizer quiet-time magnetic field model (Olson & Pfizer, 1974) is used
 109 to determine L-shell values at any given time and spacecraft location. In general, this
 110 model is appropriate at high L-shells ($L > 4.5$) during geomagnetically quiet times and
 111 at low L-shells ($L < 4.5$) during both active and quiet times. Plasmaspheric hiss, by
 112 definition, remains within the plasmasphere, and so is present at high L-shells during quiet
 113 times (extended plasmasphere) and at low L-shells during active times (eroded plasma-
 114 sphere). Therefore the Olson-Pfizer quiet-time model is appropriate for plasmaspheric
 115 hiss studies. L-shell is used instead of L^* because the relevant quantity for plasma waves
 116 is their radial distance from Earth (or the plasmopause) at the geomagnetic equator rather
 117 than a particle drift invariant (e.g Koller et al., 2009, and references therein).

118 The plasmopause is identified using the method described in Malaspina et al. (2016).
 119 This method uses plasma density derived from spacecraft potential measurements cal-
 120 ibrated each orbit against the measured upper hybrid resonance frequency, combined with
 121 the Moldwin, Downward, Rassoul, Amin, and Anderson (2002) criteria that density change
 122 by 5x or more over 0.5 L-shell. When multiple density gradients satisfying this criteria
 123 were found, the one closest to Earth is designated as the plasmopause.

124 Isolating plasmaspheric hiss wave power from all other phenomenon detected by
 125 the Van Allen Probes SCM requires excluding some data from the analysis. Data recorded
 126 at $L < 1.6$ were not considered. Data from half-orbits where no plasmopause was de-
 127 tected are excluded because ΔL_{pp} is undefined for those data. Times during spacecraft
 128 maneuvers, significant spacecraft surface charging ($|V_{sc}| > 20V$), and times when the
 129 spacecraft were in Earth eclipse were removed. Wave power > 2 kHz was excluded, as
 130 those higher frequencies contain significant contributions from lightning generated whistler-
 131 mode waves (Meredith et al., 2007), which we do not wish to include in the current model.
 132 Wave data outside the identified plasmopause L-shell or when the corresponding plasma
 133 density measurement was $< 50\text{cm}^{-3}$ were excluded from consideration, to aggressively
 134 filter out chorus wave power.

135 Several filters were applied to the remaining spectral wave data to exclude wave
 136 modes not under consideration and to separate signal from noise. Spectral bins domi-
 137 nated by magnetosonic wave power were excluded by removing from consideration spec-
 138 tral data (by time and frequency bin) with high compressability $B_{wave \parallel} / B_{wave total} >$
 139 0.6. Spectral data had to meet the following criteria: planarity > 0.2 and ellipticity $>$

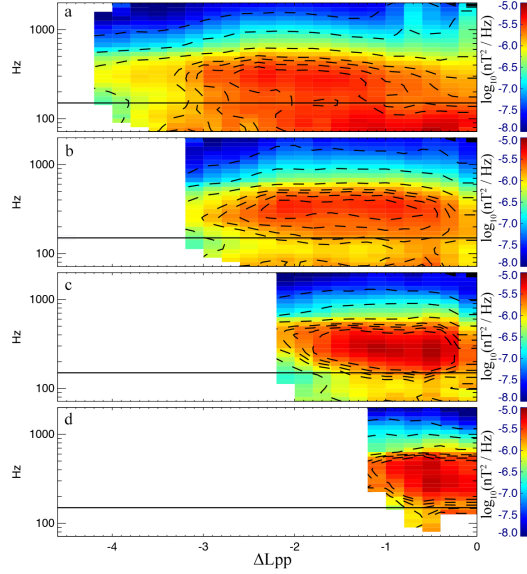
140 0.7 (Li et al., 2015) and signal to noise ≥ 5 (using the empirical SCM noise function de-
 141 rived in (Malaspina et al., 2017)). The low planarity threshold (0.2) is justified here be-
 142 cause planarity is being used only to exclude non-hiss waves (such as magnetosonic waves).
 143 A higher planarity threshold (0.5 or greater) would be required if the on-board cross-
 144 spectral data were being used to estimate wave vectors. After these exclusions, the re-
 145 maining database includes 1.9×10^8 spectral data samples.

146 2.2 Plasmaspheric Hiss Data

147 The plasmaspheric hiss data examined here are wave power spectral density (units
 148 of nT^2/Hz) binned by five quantities: frequency, distance of the plasmopause from Earth
 149 (L_{pp}), distance from the plasmopause (ΔL_{pp}), Magnetic Local Time (MLT), and the Kp
 150 geomagnetic activity index. The 65 pseudo-logarithmic spaced frequency bins defined
 151 by the EMFISIS on-board spectra are used for frequency binning. Four L_{pp} bins are used,
 152 covering the range of possible plasmopause locations observable by the Van Allen Probes:
 153 $2 \leq L_{pp} < 3$, $3 \leq L_{pp} < 4$, $4 \leq L_{pp} < 5$, and $5 \leq L_{pp} < 6$. The 25 bins for ΔL_{pp} span a
 154 range of -5 to 0, with a bin width of 0.2 L. Six MLT bins with 4 hour width are used:
 155 $0 < MLT \leq 4$, $4 < MLT \leq 8$, and so on. Finally, six Kp bins are used, where the
 156 first five have a span of 1 Kp (e.g. $0 \leq Kp < 1$, $1 \leq Kp < 2$). The final Kp bin in-
 157 cludes $Kp \geq 5$. This final bin width was selected to ensure sufficient data for meaning-
 158 ful statistics in this bin. This was necessary because geomagnetic conditions resulting
 159 in $Kp \geq 5$ are rare during the Van Allen Probes era.

160 Figure 1 shows mean values of plasmaspheric hiss wave power as a function of fre-
 161 quency and ΔL_{PP} for four different ranges of L_{PP} : Figure 1a $5 < L_{PP} \leq 6$, Figure
 162 1b $4 < L_{PP} \leq 5$, Figure 1c $3 < L_{PP} \leq 4$, Figure 1d $2 < L_{PP} \leq 3$. The data shown
 163 are for $8 < MLT \leq 12$ and $1 \leq Kp < 2$, but the data look similar for other MLT
 164 and Kp bins. Contours of amplitude are plotted over the amplitude range shown. In each
 165 case, the amplitude contours trace an elliptical shape centered at a few hundred Hz in
 166 frequency. The data show properties consistent with prior studies (e.g. (Malaspina et
 167 al., 2017)): the wave power peaks near 400 Hz, at a radial distance approximately be-
 168 tween the Earth and the plasmopause. When the plasmopause is eroded, the wave power
 169 is compressed into a smaller radial extent and the amplitude increases.

170 The thick black horizontal lines indicate 150 Hz. While wave power below 150 Hz
 171 is plotted in Figure 1, those data are not used for the plasmaspheric hiss wave model de-
 172 rived in this work. Hiss wave power below 150 Hz is considered low frequency hiss (Li
 173 et al., 2013; Ni et al., 2014; Malaspina et al., 2017), and will be considered separately
 174 in future work.



175 **Figure 1.** Mean values of observed plasmaspheric hiss wave power as a function of frequency
 176 and ΔL_{PP} for four different L_{PP} ranges, $8 < MLT \leq 12$ and $1 \leq Kp < 2$. (a) $5 < L_{PP} \leq 6$.
 177 (b) $4 < L_{PP} \leq 5$. (c) $3 < L_{PP} \leq 4$. (d) $2 < L_{PP} \leq 3$. Horizontal black lines indicate 150 Hz.
 178 Contour levels are included, indicating levels across the amplitude range shown.

179 3 Plasmapause-Parameterized Wave Model

180 Using the plasma wave data collected by the Van Allen Probes as described above,
 181 we create a plasmaspheric hiss wave model, parameterized by frequency, L_{pp} , ΔL_{pp} , and
 182 Kp.

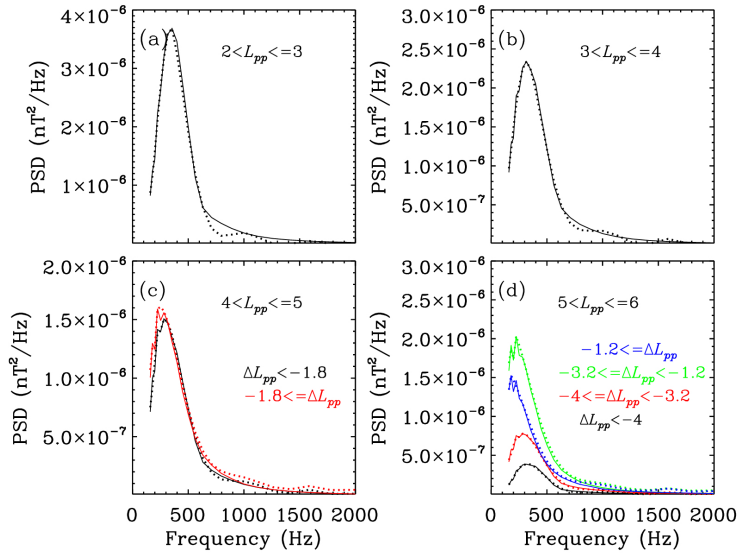
183 The shape of hiss wave power spectral density (PSD) profiles with respect to wave
 184 frequency are found to depend strongly on L_{pp} and ΔL_{pp} , and weakly on MLT and Kp.
 185 PSD profile amplitude is found to vary with L_{pp} , ΔL_{pp} , MLT, and Kp. Therefore, a pa-
 186 rameterization is chosen such that the wave model PSD frequency profile shape is de-
 187 termined by L_{pp} and ΔL_{pp} , while the appropriate amplitude scaling for that shape is
 188 determined by L_{pp} , ΔL_{pp} , MLT, and Kp.

189 To create the wave model, PSD data are first averaged over MLT and Kp. Figure
 190 2 shows these averaged PSD vs. frequency profiles (solid lines) as a function of L_{pp} and
 191 ΔL_{pp} . When PSD profiles have similar peak frequencies for different ranges of ΔL_{pp} they
 192 are combined into a single profile. The resulting PSD frequency-profiles were fit with an
 193 analytic function (dotted lines) (a piece-wise 7th order polynomial function) to facili-
 194 tate diffusion coefficient calculations. Fits are carried out separately for frequency ranges
 195 before and after the maxima of the PSD profiles f_{peak} as follows:

$$\text{PSD}(f) = \begin{cases} \sum_{n=0}^7 a_n f^n & (f < f_{\text{peak}}) \\ \sum_{n=0}^7 b_n f^n & (f \geq f_{\text{peak}}) \end{cases} \quad (1)$$

196 We then normalize over the obtained PSD profiles such that the wave amplitude
 197 is unity when integrated over the frequency range from 150 Hz to 2000 Hz.

198 All values of f_{peak} and fitted polynomial coefficients can be found in Table 1. The
 199 wave amplitude scaling appropriate to each normalized PSD profiles is obtained by com-
 200 parison with the observational hiss database. This combination of PSD profile fitting and
 201 wave amplitude scaling allows us to fully parameterize the hiss wave distributions.

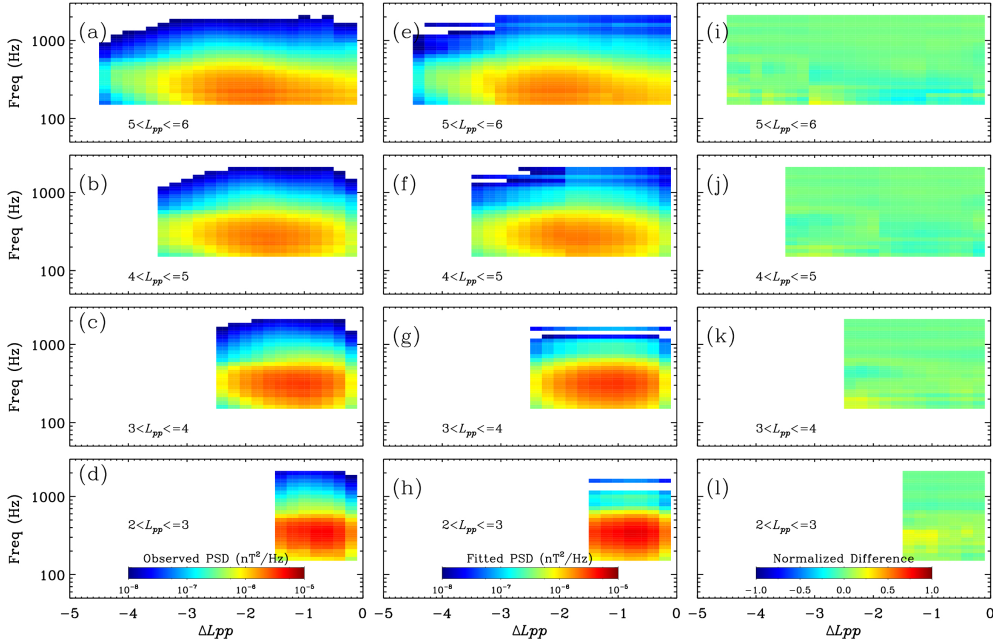


202 **Figure 2.** PSD (nT^2/Hz) sorted by L_{pp} and ΔL_{pp} (solid lines) and 7th order polynomial
 203 piece-wise fitting (dotted lines), for four ranges of L_{pp} (a-d) and ΔL_{pp}

204 Figure 3 shows the comparison between the observed and parameterized hiss wave
 205 power distributions and their normalized difference as functions of ΔL_{pp} and L_{pp} . The
 206 normalized difference is defined as

$$\text{ND}(f, \Delta L_{pp}) = \frac{2(PSD_{fitted}(f, \Delta L_{pp}) - PSD_{observed}(f, \Delta L_{pp}))}{\max(PSD_{fitted}(f, \Delta L_{pp}) + PSD_{observed}(f, \Delta L_{pp}))} \quad (2)$$

207 It is shown that the observed PSD distributions of hiss wave power are well-modeled
 208 by the fitting results and the normalized differences between the fits and observations
 209 are close to zero.



210 **Figure 3.** Observed (a-d) and fitted (e-h) power spectral density distributions of plasmaspheric hiss waves and their normalized difference (i-l) as function of ΔL_{pp} and L_{pp} averaged over
 211 MLT and Kp
 212

213 In addition to the L_{pp} -sorted wave model, a traditional hiss wave model was constructed based on the same wave data (parameterized by L-shell, instead of ΔL_{pp} and
 214 L_{pp}). PSD frequency profiles and amplitude scalings were obtained using methodology
 215 analogous to that described for the L_{pp} -sorted model.
 216

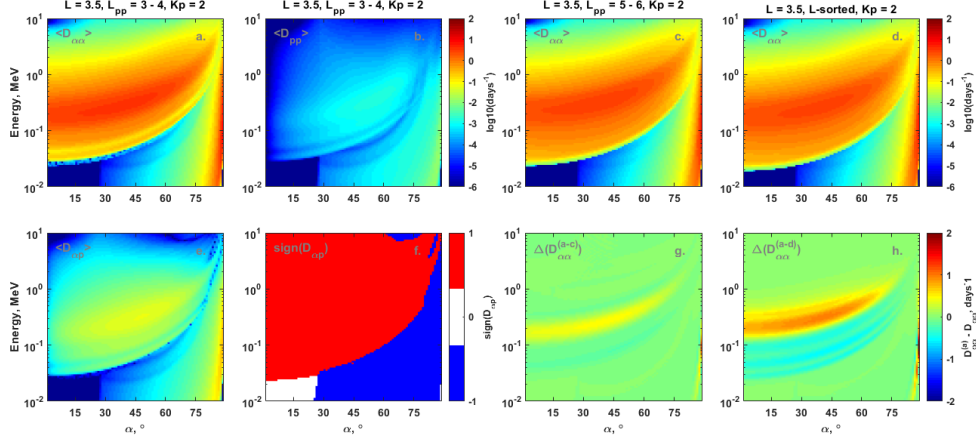
4 Diffusion Coefficient Calculations

The Full Diffusion Code (FDC) (Ni et al., 2008; Shprits & Ni, 2009) is used to calculate plasmaspheric hiss diffusion coefficients. The polynomial fits of the observed L_{pp} -sorted hiss PSD profiles described in Section 3 are used as frequency inputs into the code. The Denton et al. (2006) model is used to define plasma number density. The wave normal distribution is assumed to be a Gaussian distribution (Glauert & Horne, 2005) with a peak at $\tan(0^\circ)$, a width $\tan(30^\circ)$, a lower cutoff $\tan(0^\circ)$ and an upper cutoff $\tan(45^\circ)$. The resonance orders from -5 to 5, including 0 order, are considered.

Diffusion matrices at specific values of L-shell and Kp-index are multiplied by the hiss wave amplitude scaling factors determined for the corresponding L_{pp} , ΔL_{pp} , and Kp. Diffusion matrices are averaged over MLT. Using analogous methodology, diffusion coefficients are also calculated for the L -sorted hiss wave model PSD profiles.

Figures 4a, b, e, f show an example of calculated pitch-angle ($D_{\alpha\alpha}$), energy (D_{pp}), mixed ($D_{\alpha p}$) diffusion coefficients, as well as the the sign of the mixed term, for the L_{pp} -sorted hiss model at fixed $L = 3.5$, $Kp = 2$ and $3 < L_{pp} \leq 4$. As expected, the energy diffusion coefficient of the hiss waves is relatively small in comparison to the pitch angle diffusion coefficient. Figure 4c shows the pitch angle diffusion coefficient at the same L-shell and Kp-index but for a different plasmopause location $4 < L_{pp} \leq 5$. The difference between pitch angle diffusion coefficients (Figure 4g, difference between Figure 4a and Figure 4c) indicates that stronger scattering by hiss waves when the plasmopause is closer Earth primarily affects electrons with energies from 100 keV to 1 MeV.

Figure 4d shows pitch angle diffusion coefficients for the hiss model constructed using traditional L -sorted methodology. The difference between pitch angle diffusion coefficients from L_{pp} -sorted and L -sorted models (Figure 4h, difference between 4a and 4d) is clear, for the same range of electron energies. The differences reach $\sim 2 \text{ days}^{-1}$. Thus, the one can expect that electron distribution dynamics in diffusion simulations will depend on the wave data parameterization (sorting) approach of the hiss model (L -sorted vs L_{pp} -sorted). In addition, the variation can be significant on the timescales of geomagnetic storms (a few days).



246 **Figure 4.** (a,b,e) Calculated diffusion coefficients for L_{pp} -sorted plasmaspheric hiss waves
 247 model $3 < L_{pp} \leq 4$, (f) Sign of $D_{\alpha p}$, (c) $D_{\alpha\alpha}$, $5 < L_{pp} \leq 6$, (d) $D_{\alpha\alpha}$, L -sorted hiss model. (g, h)
 248 Difference of panels c and d with panel a.

249 5 Pitch angle diffusion simulations

250 To quantify the impact of the wave data sorting approach on modeling results, we
 251 perform VERB code simulations in 1D mode using pitch-angle diffusion only. This ap-
 252 proach allows us to focus on the impact that different hiss wave models may have on the
 253 simulation as we ignore other processes such as radial diffusion. Since the electron ac-
 254 celeration by hiss waves is ineffective, we ignore energy diffusion. Neglecting radial and
 255 energy diffusion, the Fokker-Planck equation (Schulz & Lanzerotti, 1974) that describes
 256 the evolution phase space density (f) can be written as:

$$\frac{\partial f}{\partial t} = \frac{1}{T(\sin(\alpha)) \sin(2\alpha)} \frac{\partial}{\partial \alpha} T(\sin(\alpha)) \sin(2\alpha) D_{\alpha\alpha} \frac{\partial f}{\partial \alpha} - \frac{f}{\tau}$$

257 where $T(\sin(\alpha)) \approx 1.38 - 0.32(\sin(\alpha) + \sqrt{\sin(\alpha)})$ is a function that corresponds
 258 to the bounce frequency, approximated following Lenchek, Singer, and Wentworth (1961),
 259 α is the equatorial pitch angle, $D_{\alpha\alpha}$ is the pitch angle diffusion coefficient, τ defines the
 260 lifetime of the particle inside the loss cone where it is equal to quarter of the bounce pe-
 261 riod.

262 We perform simulations on a grid of $\alpha \in [0.1^\circ, 89.5^\circ]$ linearly distributed among
 263 101 points. The Dirichlet boundary condition is equal to zero at $\alpha = 0.1^\circ$ and the Neu-
 264 mann boundary condition is the derivative equal to zero at $\alpha = 89.5^\circ$. The initial con-
 265 dition is an isotropic phase space density distribution ($f(\alpha) = 1$). The energy of the

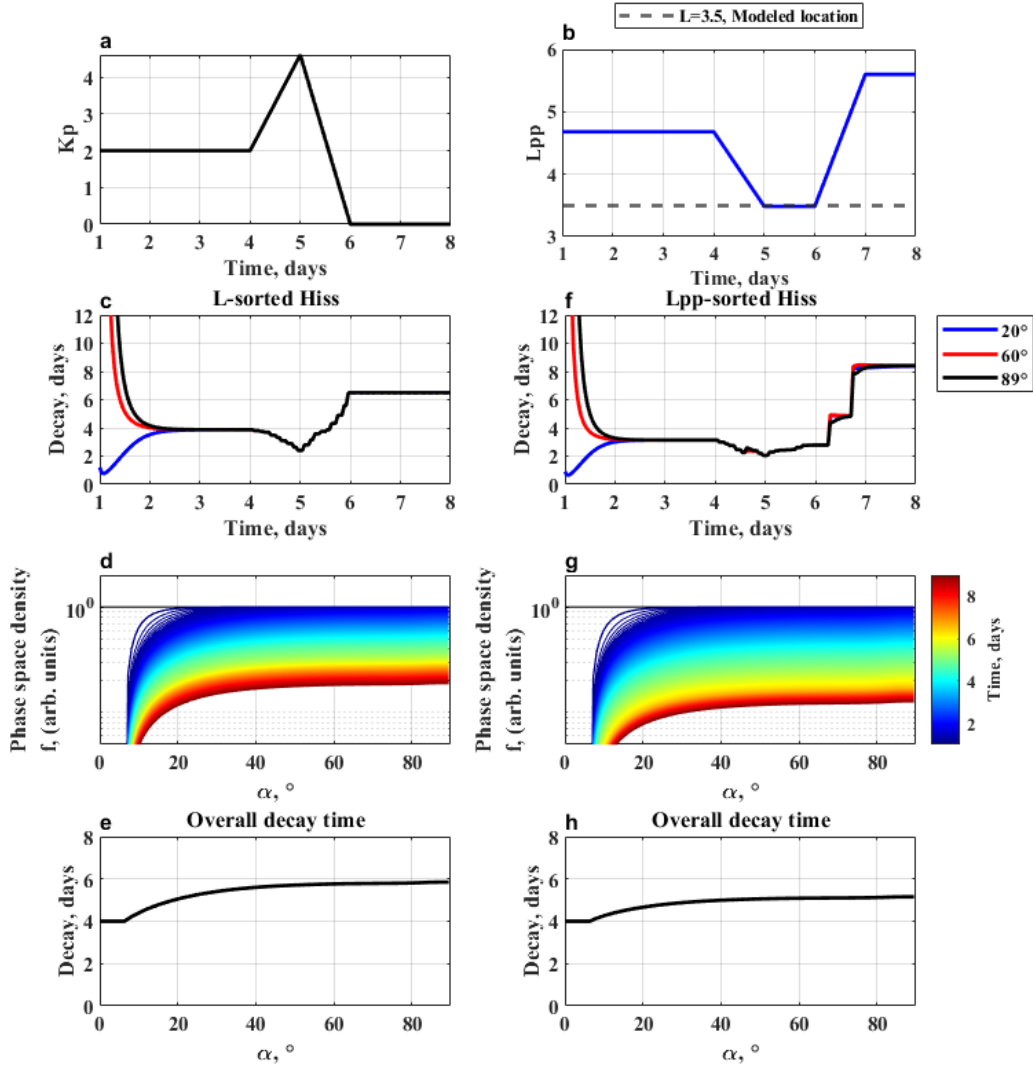
266 electrons is 1 MeV. A similar simulation setup was used in previous studies (e.g. Shprits
267 et al., 2009).

268 Figure 5 shows the results of two simulations at fixed L-shell equal to 3.5. These
269 simulations are distinguished by the use of two models for hiss waves described above
270 (L -sorted and L_{pp} -sorted). Different diffusion coefficients are applied for each wave model.
271 Both simulations were performed for 7 days, using a prescribed variation of the Kp-index
272 during an idealized geomagnetic storm (Figure 5a). The plasmopause location is deter-
273 mined based on Kp following Carpenter and Anderson (1992) (Figure 5b).

274 To compare the results of the simulations, decay rates are calculated at different
275 pitch angles ($20^\circ, 60^\circ, 89^\circ$ in Figures 5c, f) and overall decay times are calculated follow-
276 ing the technique described in Shprits, Li, and Thorne (2006) (Figures 5e, h). The de-
277 cay rates are controlled by the electron phase space density gradient and the diffusion
278 rate at the edge of the loss cone (see Shprits et al., 2006).

279 Both simulations are given an initial 4 day period of constant $Kp = 2$, which cor-
280 responds to a constant location of the plasmopause at $L_{pp} = 4.68$. During this period,
281 the diffusion coefficients are held constant in both simulations as the simulations reach
282 steady state conditions (no change in phase space density gradient, see Figure 5c, d). Hence,
283 the electron dynamics of the remainder of the modeled time period are defined by vari-
284 ation of the diffusion coefficients, which are determined by the wave data sorting approach,
285 L_{pp} - vs L -sorted). The idealized geomagnetic storm starts on day 4 with increasing Kp-
286 index and corresponding compression of the plasmopause spanning one day. On day 5,
287 the Kp-index is allowed to decrease, followed by an expansion of the plasmopause on day
288 6. Such conditions are typical for geomagnetic storms.

295 Comparison of the simulation results shows that the electron decay rate evolution
296 during the storm time is noticeably different (see Figure 5c, f). The difference is also vis-
297 ible in evolution of the phase space density profiles for 1 MeV electrons (see Figure 5d,
298 g). The step-like increases of decay rate in Figure 5f are the consequence of the small
299 number (4) of discrete L_{pp} bins that are used to calculate the diffusion coefficients. The
300 small number of bins is due to statistical limitations of the wave data. The presence of
301 these steps does not alter the clear difference in the simulated electron dynamics found
302 by using different hiss models.



289 **Figure 5.** One-dimensional modeling of idealized geomagnetic storm at $L=3.5$. (a) Kp-index.
 290 (b) Location of the plasmapause. (c, d, e) Results of the simulation with the L -sorted hiss model.
 291 (f, g, h) Results of the simulation with the L_{pp} -sorted hiss model. (c, f) Evolution of decay time
 292 during the storm. (d, g) Evolution of the pitch angle distribution for 1 MeV electrons (phase
 293 space density). (e, h) Overall decay time as a function of the equatorial pitch angle, calculated
 294 using initial and final phase space density profiles.

303 Based on these results, it is expected that a simulation of a realistic storm using
 304 the L_{pp} -sorted hiss model will result in different electron dynamics on the time scale of
 305 the duration of the storm (days) compared to simulations using traditional L -sorted hiss

306 wave models. Simulations using the L_{pp} -sorted hiss model may reveal otherwise-hidden
 307 variation of the electron distribution during storms and may also lead to a different sim-
 308 ulated balance between acceleration and loss processes due to changes in the phase space
 309 density gradient. However, pitch angle scattering by hiss waves is only one of many pro-
 310 cesses that define the dynamics of the electrons. Future simulations will include contri-
 311 butions from other very low frequency (VLF) waves via pitch-angle, energy, mixed dif-
 312 fusion, and radial diffusion driven by ultra-low frequency (ULF) waves.

313 6 Conclusion

314 In this study, Van Allen Probes observations of plasmaspheric hiss (organized by
 315 frequency, ΔL_{pp} , L_{pp} , MLT, and K_p) were compiled for the time period 2012 - 2018. From
 316 these data, an empirical hiss wave model was constructed for hiss parameterized by ΔL_{pp} ,
 317 L_{PP} , and K_p . Corresponding pitch-angle and energy diffusion coefficients (including mixed-
 318 terms) were calculated.

319 The pitch angle diffusion coefficients for the L_{pp} -sorted empirical hiss model showed
 320 significant differences when compared with diffusion coefficients calculated for the same
 321 L-shell but using traditional L -sorted hiss parameterization.

322 A 1D mode of the VERB code with idealized geomagnetic storm conditions was
 323 used to quantify differences in electron lifetimes as determined using diffusion coefficients
 324 calculated using the L_{pp} -sorted hiss wave model and the L -sorted hiss wave model. Clear
 325 differences were found over time timescales of the geomagnetic storm (few days).

326 Future studies will expand upon the current model by (i) simulating more realis-
 327 tic geomagnetic variation time-histories, (ii) utilizing the 3D mode of the VERB code,
 328 and (iii) developing L_{pp} -sorted parameterizations for other hiss types such as exohiss and
 329 low frequency hiss.

330 Acknowledgments

331 The authors thank the Van Allen Probes team, especially the EFW and EMFISIS teams
 332 for their support. This work was funded by NASA grant 80NSSC18K1034. All Van Allen
 333 Probes data used in this work are available from the EFW and EMFISIS team websites,
 334 which one can link to here: <http://rbspgateway.jhuapl.edu>. The diffusion coefficients, wave
 335 amplitude scaling, and the VERB code are available on <ftp://rbm.epss.ucla.edu/>.

Table 1. The values of f_{peak} and the fitted polynomial coefficients of plasmaspheric hiss waves as functions of L_{pp} and ΔL_{pp} .

L_{pp} ranges	ΔL_{pp} ranges	f_{peak} (Hz)	a_0	a_1	a_2	a_3	a_4	a_5	a_6	a_7
			b_0	b_1	b_2	b_3	b_4	b_5	b_6	b_7
$2 < L_{pp} \leq 3$	$\Delta L_{pp} < 0$	355	6.59e-3	-3.41e-4	6.98e-6	-7.24e-8	4.19e-10	-1.35e-12	2.29e-15	-1.58e-18
			-2.99e-2	3.17e-4	-1.15e-6	2.05e-9	-2.02e-12	1.13e-15	-3.33e-19	4.04e-23
$3 < L_{pp} \leq 4$	$\Delta L_{pp} < 0$	316	9.29e-3	-4.81e-4	1.01e-5	-1.08e-7	6.64e-10	-2.31e-12	4.25e-15	-3.22e-18
			-1.97e-2	2.16e-4	-7.88e-7	1.41e-9	-1.39e-12	7.79e-16	-2.30e-19	2.78e-23
$4 < L_{pp} \leq 5$	$\Delta L_{pp} < -1.8$	282	-2.23e-2	1.29e-3	-2.93e-5	3.54e-7	-2.45e-9	9.76e-12	-2.08e-14	1.83e-17
			-1.18e-2	1.46e-4	-5.50e-7	9.97e-10	-9.92e-13	5.55e-16	-1.64e-19	1.99e-23
$4 < L_{pp} \leq 5$	$-1.8 \leq \Delta L_{pp} < 0$	224	-8.68e-2	5.41e-3	-1.39e-4	1.94e-6	-1.56e-8	7.31e-11	-1.85e-13	1.95e-16
			-4.46e-3	7.73e-5	-3.13e-7	5.86e-10	-5.96e-13	3.39e-16	-1.01e-19	1.24e-23
$5 < L_{pp} \leq 6$	$\Delta L_{pp} < -4$	316	8.31e-3	-4.30e-4	8.76e-6	-9.13e-8	5.35e-10	-1.77e-12	3.07e-15	-2.19e-18
			-2.96e-2	3.00e-4	-1.07e-6	1.88e-9	-1.85e-12	1.03e-15	-3.02e-19	3.65e-23
$5 < L_{pp} \leq 6$	$-4 \leq \Delta L_{pp} < -3.2$	282	-2.00e-2	1.11e-3	-2.53e-5	3.07e-7	-2.14e-9	8.55e-12	-1.83e-14	1.61e-17
			-1.28e-2	1.56e-4	-5.87e-7	1.07e-9	-1.07e-12	5.98e-16	-1.77e-19	2.15e-23
$5 < L_{pp} \leq 6$	$-3.2 \leq \Delta L_{pp} < -1.2$	224	-1.09e-1	6.90e-3	-1.80e-4	2.51e-6	-2.04e-8	9.60e-11	-2.43e-13	2.57e-16
			7.76e-4	3.57e-5	-1.84e-7	3.78e-10	-4.03e-13	2.37e-16	-7.23e-20	8.99e-24
$5 < L_{pp} \leq 6$	$-1.2 \leq \Delta L_{pp} < 0$	178	8.33e-2	-4.39e-3	8.88e-5	-7.95e-7	1.95e-9	1.74e-11	-1.29e-13	2.52e-16
			1.80e-3	2.68e-5	-1.62e-7	3.61e-10	-4.08e-13	2.50e-16	-7.92e-20	1.02e-23

References

- 336
- 337 Albert, J. M., Meredith, N. P., & Horne, R. B. (2009). Three-dimensional diffusion
 338 simulation of outer radiation belt electrons during the 9 october 1990 magnetic
 339 storm. *J. Geophys. Res. [Space Phys]*, *114*(A9). doi: 10.1029/2009JA014336
- 340 Carpenter, D. L., & Anderson, R. R. (1992, February). An ISEE/Whistler model of
 341 equatorial electron density in the magnetosphere. *Journal of Geophysical Re-*
 342 *search (Space Physics)*, *97*, 1097-1108. doi: 10.1029/91JA01548
- 343 Carpenter, D. L., & Lemaire, J. (2004, December). The Plasmasphere Boundary
 344 Layer. *Annales Geophysicae*, *22*, 4291-4298. doi: 10.5194/angeo-22-4291-2004
- 345 Denton, R. E., Takahashi, K., Galkin, I. A., Nsumei, P. A., Huang, X., Reinisch,
 346 B. W., . . . Hughes, W. J. (2006). Distribution of density along magnetospheric
 347 field lines. *J. Geophys. Res.*, *111*, A04213. doi: 10.1029/2005JA011414
- 348 Fok, M.-C., Buzulukova, N. Y., Chen, S.-H., Glocer, A., Nagai, T., Valek, P., &
 349 Perez, J. D. (2014, September). The Comprehensive Inner Magnetosphere-
 350 Ionosphere Model. *Journal of Geophysical Research (Space Physics)*, *119*,
 351 7522-7540. doi: 10.1002/2014JA020239
- 352 Glauert, S. A., & Horne, R. B. (2005). Calculation of pitch angle and energy dif-
 353 fusion coefficients with the padie code. *Journal of Geophysical Research: Space*
 354 *Physics*, *110*(A4).
- 355 Glauert, S. A., Horne, R. B., & Meredith, N. P. (2014, January). Three-dimensional
 356 electron radiation belt simulations using the BAS Radiation Belt Model with
 357 new diffusion models for chorus, plasmaspheric hiss, and lightning-generated
 358 whistlers. *Journal of Geophysical Research (Space Physics)*, *119*, 268-289. doi:
 359 10.1002/2013JA019281
- 360 Jordanova, V. K., & Miyoshi, Y. (2005, 28 July). Relativistic model of ring cur-
 361 rent and radiation belt ions and electrons: Initial results: RADIATION
 362 BELT IONS AND ELECTRONS. *Geophys. Res. Lett.*, *32*(14). doi:
 363 10.1029/2005GL023020
- 364 Kletzing, C. A., Kurth, W. S., Acuna, M., MacDowall, R. J., Torbert, R. B.,
 365 Averkamp, T., . . . Tyler, J. (2013, November). The Electric and Magnetic
 366 Field Instrument Suite and Integrated Science (EMFISIS) on RBSP. *Space*
 367 *Science Reviews*, *179*, 127-181. doi: 10.1007/s11214-013-9993-6
- 368 Koller, J., Reeves, G. D., & Friedel, R. H. W. (2009, Feb). LANL* V1.0: a radiation

- 369 belt drift shell model suitable for real-time and reanalysis applications. *Geosci-*
 370 *entific Model Development Discussions*, 2(1), 159-184.
- 371 Lenchek, A. M., Singer, S. F., & Wentworth, R. C. (1961, Dec). Geomagnetically
 372 Trapped Electrons from Cosmic-Ray Albedo Neutrons. *Journal of Geophysical*
 373 *Research*, 66(12), 4027-4046. doi: 10.1029/JZ066i012p04027
- 374 Li, W., Ma, Q., Thorne, R. M., Bortnik, J., Kletzing, C. A., Kurth, W. S., ...
 375 Nishimura, Y. (2015, May). Statistical properties of plasmaspheric hiss de-
 376 rived from Van Allen Probes data and their effects on radiation belt electron
 377 dynamics. *Journal of Geophysical Research (Space Physics)*, 120, 3393-3405.
 378 doi: 10.1002/2015JA021048
- 379 Li, W., Shen, X. C., Ma, Q., Capannolo, L., Shi, R., Redmon, R. J., ... Hospo-
 380 darsky, G. B. (2019, Apr). Quantification of Energetic Electron Precipitation
 381 Driven by Plume Whistler Mode Waves, Plasmaspheric Hiss, and Exohiss.
 382 *Geophysical Research Letters*, 46(7), 3615-3624. doi: 10.1029/2019GL082095
- 383 Li, W., Thorne, R. M., Bortnik, J., Reeves, G. D., Kletzing, C. A., Kurth, W. S., ...
 384 Thaller, S. A. (2013, August). An unusual enhancement of low-frequency plas-
 385 maspheric hiss in the outer plasmasphere associated with substorm-injected
 386 electrons. *Geophysical Review Letters*, 40, 3798-3803. doi: 10.1002/grl.50787
- 387 Malaspina, D. M., Jaynes, A. N., Boulé, C., Bortnik, J., Thaller, S. A., Ergun, R. E.,
 388 ... Wygant, J. R. (2016, August). The distribution of plasmaspheric hiss wave
 389 power with respect to plasmopause location. *Geophysical Review Letters*, 43,
 390 7878-7886. doi: 10.1002/2016GL069982
- 391 Malaspina, D. M., Jaynes, A. N., Hospodarsky, G., Bortnik, J., Ergun, R. E., &
 392 Wygant, J. (2017, August). Statistical properties of low-frequency plasmas-
 393 pheric hiss. *Journal of Geophysical Research (Space Physics)*, 122, 8340-8352.
 394 doi: 10.1002/2017JA024328
- 395 Malaspina, D. M., Ripoll, J.-F., Chu, X., Hospodarsky, G., & Wygant, J. (2018,
 396 September). Variation in Plasmaspheric Hiss Wave Power With Plasma
 397 Density. *Geophysical Research Letters*, 45, 9417-9426. doi: 10.1029/
 398 2018GL078564
- 399 Mauk, B. H., Fox, N. J., Kanekal, S. G., Kessel, R. L., Sibeck, D. G., & Ukhorskiy,
 400 A. (2013, November). Science Objectives and Rationale for the Radia-
 401 tion Belt Storm Probes Mission. *Space Science Reviews*, 179, 3-27. doi:

- 402 10.1007/s11214-012-9908-y
- 403 Meredith, N. P., Horne, R. B., Glauert, S. A., & Anderson, R. R. (2007, August).
404 Slot region electron loss timescales due to plasmaspheric hiss and lightning-
405 generated whistlers. *Journal of Geophysical Research (Space Physics)*, *112*,
406 8214. doi: 10.1029/2007JA012413
- 407 Millan, R. M., & Thorne, R. M. (2007, March). Review of radiation belt relativistic
408 electron losses. *Journal of Atmospheric and Solar-Terrestrial Physics*, *69*, 362-
409 377. doi: 10.1016/j.jastp.2006.06.019
- 410 Miyoshi, Y. S., Jordanova, V. K., Morioka, A., Thomsen, M. F., Reeves, G. D.,
411 Evans, D. S., & Green, J. C. (2006, 1 November). Observations and modeling
412 of energetic electron dynamics during the october 2001 storm. *J. Geophys.*
413 *Res.*, *111*(A11), A11S02. doi: 10.1029/2005JA011351
- 414 Moldwin, M. B., Downward, L., Rassoul, H. K., Amin, R., & Anderson, R. R. (2002,
415 November). A new model of the location of the plasmopause: CRRES re-
416 sults. *Journal of Geophysical Research (Space Physics)*, *107*, 1339. doi:
417 10.1029/2001JA009211
- 418 Ni, B., Li, W., Thorne, R. M., Bortnik, J., Ma, Q., Chen, L., . . . Claudepierre,
419 S. G. (2014, March). Resonant scattering of energetic electrons by un-
420 usual low-frequency hiss. *Geophysical Review Letters*, *41*, 1854-1861. doi:
421 10.1002/2014GL059389
- 422 Ni, B., Thorne, R. M., Shprits, Y. Y., & Bortnik, J. (2008). Resonant scatter-
423 ing of plasma sheet electrons by whistler-mode chorus: Contribution to dif-
424 fuse auroral precipitation. *Geophysical Research Letters*, *35*(11). Retrieved
425 from [https://agupubs.onlinelibrary.wiley.com/doi/abs/10.1029/](https://agupubs.onlinelibrary.wiley.com/doi/abs/10.1029/2008GL034032)
426 [2008GL034032](https://agupubs.onlinelibrary.wiley.com/doi/abs/10.1029/2008GL034032) doi: 10.1029/2008GL034032
- 427 Olson, W. P., & Pfizter, K. A. (1974). A quantitative model of the magnetospheric
428 magnetic field. *Journal of Geophysical Research (Space Physics)*, *79*, 3739. doi:
429 10.1029/JA079i025p03739
- 430 Orlova, K., Shprits, Y., & Spasojevic, M. (2016, February). New global loss model
431 of energetic and relativistic electrons based on Van Allen Probes measure-
432 ments. *Journal of Geophysical Research (Space Physics)*, *121*, 1308-1314. doi:
433 10.1002/2015JA021878
- 434 Orlova, K., Spasojevic, M., & Shprits, Y. (2014, June). Activity-dependent global

- 435 model of electron loss inside the plasmasphere. *Geophysical Review Letters*, *41*,
436 3744-3751. doi: 10.1002/2014GL060100
- 437 Schulz, M., & Lanzerotti, L. J. (1974). *Particle diffusion in the radiation belts*.
- 438 Shprits, Y. Y., Chen, L., & Thorne, R. M. (2009). Simulations of pitch angle scat-
439 tering of relativistic electrons with mlt-dependent diffusion coefficients. *Journal*
440 *of Geophysical Research: Space Physics*, *114*(A3). Retrieved from [https://](https://agupubs.onlinelibrary.wiley.com/doi/abs/10.1029/2008JA013695)
441 agupubs.onlinelibrary.wiley.com/doi/abs/10.1029/2008JA013695 doi:
442 10.1029/2008JA013695
- 443 Shprits, Y. Y., Li, W., & Thorne, R. M. (2006). Controlling effect of the pitch an-
444 gle scattering rates near the edge of the loss cone on electron lifetimes. *Journal*
445 *of Geophysical Research: Space Physics*, *111*(A12). Retrieved from [https://](https://agupubs.onlinelibrary.wiley.com/doi/abs/10.1029/2006JA011758)
446 agupubs.onlinelibrary.wiley.com/doi/abs/10.1029/2006JA011758 doi:
447 10.1029/2006JA011758
- 448 Shprits, Y. Y., & Ni, B. (2009). Dependence of the quasi-linear scattering
449 rates on the wave normal distribution of chorus waves. *Journal of Geo-*
450 *physical Research: Space Physics*, *114*(A11). Retrieved from [https://](https://agupubs.onlinelibrary.wiley.com/doi/abs/10.1029/2009JA014223)
451 agupubs.onlinelibrary.wiley.com/doi/abs/10.1029/2009JA014223 doi:
452 10.1029/2009JA014223
- 453 Shprits, Y. Y., Subbotin, D. A., Meredith, N. P., & Elkington, S. R. (2008, Novem-
454 ber). Review of modeling of losses and sources of relativistic electrons in the
455 outer radiation belt II: Local acceleration and loss. *Journal of Atmospheric*
456 *and Solar-Terrestrial Physics*, *70*, 1694-1713. doi: 10.1016/j.jastp.2008.06.014
- 457 Subbotin, D. A., & Shprits, Y. Y. (2009, October). Three-dimensional modeling of
458 the radiation belts using the Versatile Electron Radiation Belt (VERB) code.
459 *Space Weather*, *7*, S10001. doi: 10.1029/2008SW000452
- 460 Tsurutani, B. T., Falkowski, B. J., Pickett, J. S., Santolik, O., & Lakhina, G. S.
461 (2015, January). Plasmaspheric hiss properties: Observations from Po-
462 lar. *Journal of Geophysical Research (Space Physics)*, *120*, 414-431. doi:
463 10.1002/2014JA020518
- 464 Wygant, J. R., Bonnell, J. W., Goetz, K., Ergun, R. E., Mozer, F. S., Bale, S. D.,
465 ... Tao, J. B. (2013, November). The Electric Field and Waves Instruments
466 on the Radiation Belt Storm Probes Mission. *Space Science Reviews*, *179*,
467 183-220. doi: 10.1007/s11214-013-0013-7

- 468 Zhu, H., Gu, W., & Chen, L. (2019). Statistical analysis on plasmatrough exo-
469 hiss waves from the van allen probes. *Journal of Geophysical Research: Space*
470 *Physics*, *124*(6), 4356–4364.
- 471 Zhu, H., Su, Z., Xiao, F., Zheng, H., Wang, Y., Shen, C., . . . Baker, D. N. (2015,
472 February). Plasmatrough exohiss waves observed by Van Allen Probes:
473 Evidence for leakage from plasmasphere and resonant scattering of radi-
474 ation belt electrons. *Geophysical Review Letters*, *42*, 1012-1019. doi:
475 10.1002/2014GL062964